On the localisation of damage under pure bending using a nonlocal approach

F. Suárez[a]

[a]*Department of Mechanics, Faculty of Civil Engineering, Czech Technical University in Prague, Thákurova 7, 166 29, Prague 6, Czech Republic*

Abstract

To reproduce the behaviour of quasibrittle materials mathematically, constitutive laws with softening are needed, which often leads to development of damage localisation bands. If a standard local formulation is used, this approach shows a high mesh-dependence, which can be mitigated by making use of alternative nonlocal formulations. The aim of this paper is to assess the localisation properties of damage models under pure bending using different nonlocal formulations; to permit a partially analytical treatment, the idealised case of pure bending is studied. Under these conditions, the localisation process starts at the tensile face of the beam, which belongs to the boundary of the domain on which the problem is solved. Consequently, localisation patterns are affected by the boundary treatment as well as other parameters, such as the characteristic length that defines the area contributing to the nonlocal averaging. This paper presents an analytical study of the onset of localisation of different nonlocal formulations for a beam under pure bending. In addition to it, the subsequent evolution of the localised solution is explored by numerical simulations, analysing the localisation bands spacing, the dissipated energy profile along the fracture plane and the Moment-$\frac{\phi}{L}$ diagrams, with $\frac{\phi}{L}$ being a parameter that represents the rotation that drives the loading process. An analysis of damage localisation on longer

*F. Suárez
Email address: fsuarez@ujaen.es (F. Suárez)
Present address: Departamento de Ingeniería Mecánica y Minera. Universidad de Jaén. Campus Científico-Tecnológico de Linares. Cinturón Sur 23700-Linares (Jaén)

beams where damage localises in several areas is also carried out and, finally, the damage localisation due to shrinkage is studied as a more realistic example of the problem addressed here.

Keywords: Damage, Localisation, Nonlocal models, Boundary effects, Pure bending

1. Introduction

Concrete is the most extended material in construction and, although studied for many decades, still gives rise to new developments and research. In particular, the time-dependent behaviour of concrete due to creep and shrinkage is an issue still under study, where many researchers are proposing methods and models to mathematically reproduce this process due to drying and aging [1, 2, 3, 4, 5, 6, 7]. Drying shrinkage on a concrete surface produces a uniformly distributed strain field on the element, which is a similar situation to a beam subjected to pure bending, where strain also varies in parallel planes. In this paper, the pure bending problem is used to study how different nonlocal formulations predict damage initiation and evolution, as an approach to the problem of shrinkage and creep.

In continuum damage mechanics, the use of constitutive laws with softening is widely extended to mathematically reproduce the behaviour observed with experiments. This type of models, when formulated locally, show a pathological dependence on the elements size. This issue can be addressed by simple adjustments that make some constitutive parameters dependent on the element size or by making use of more sophisticated enhancements that introduce an internal length, e.g. based on integral-type or gradient-type nonlocal formulations.

Unlike local schemes, nonlocal formulations evaluate the stress at each integration point using a state variable computed as a weighted average of the values at neighbour integration points, which leads to a much smaller mesh-dependence compared with local formulations. An overview of these methods can be found at [8] and [9].

Different alternatives can be used when defining a nonlocal formulation, e.g. using different weight functions to compute the contribution of each neighbour point to the nonlocal average. Nevertheless, one of the most interesting aspects of this problem is how to deal with nonlocal averaging near a body boundary; a good study on this topic can be found in [10]. As shown by Jirásek et al. in [11] and analysed by Grassl et al. in [12], using standard averaging procedures may result in excessive spurious energy dissipation close to boundaries for notched specimens. To reduce these effects, alternative approaches have been proposed to obtain the average nonlocal value, some making the weight functions dependent on the distance to the boundary [13, 14, 15] and some making them dependent on the stress state [16, 17, 18]. Here, another interesting approach will be used, which was proposed by Polizzotto [19] and Borino et al. [20] and which will be referred to as the local complement method.

The aim of the present paper is to assess the localisation properties of nonlocal damage models under bending. To permit a partially analytical study and to display the fundamental properties of various formulations, the idealised case of uniform bending is studied. Therefore, the beam is considered to have a constant cross section and to be subjected to a uniformly distributed bending moment and zero normal force.

Five boundary treatments to compute the nonlocal values near the body boundaries are compared: standard scaling, local complement, stress-based approach and two distance-based approaches. Furthermore, three weight functions are utilised to obtain the nonlocal values and their performance compared.

To analyse the possible combinations of boundary treatments and weight functions, two approaches are used. First, a simple analytical model is developed to observe how each of them computes the nonlocal strain profile of the beam cross-section under elastic conditions. This helps to understand why damage is developed earlier in some cases and helps to decide which alternative is more accurate compared to the expected theoretical strain profile.

In addition to the analytical study, a finite element model is built to study the problem. This model represents an infinite beam under pure bending; to

do so, periodic boundary conditions are defined. This model is computed for several averaging schemes and several values of the characteristic length R to compare how each of them affects the localisation pattern. The localisation bands spacing is analysed, together with the Moment-$\frac{\phi}{L}$ diagram, with $\frac{\phi}{L}$ being the parameter representing the rotation that drives the loading process in the model, and the dissipated energy profile along the cross-section where damage is developed. Additionally, the evolution of damage on longer beams, where localisation takes place in several areas at the same time, is addressed.

Finally, to study a more realistic problem, an example of the effect of shrinkage on the localisation of damage is presented, which is a common situation in most concrete structures and produces similar effects as pure bending on the problem. This is carried out using a staggered scheme, that is to say, computing two physical models in parallel; the first one reproduces shrinkage and feeds the second model, which reproduces damage evolution as a consequence of strains due to shrinkage.

2. Nonlocal formulations

When using local formulations of damage models, there exists a mesh-dependence that makes it difficult to ensure that the result obtained is fully representative of the problem under consideration. To avoid this problem, nonlocal formulations allow to evaluate damage using nonlocal values of strain, that is to say, using a value of the equivalent strain computed as an average value of the Gauss point under consideration and those neighbours at a distance that is defined by a parameter with the dimension of length, usually referred to as the nonlocal characteristic length, which will be here denoted as R, following the notation by Grassl et al. [12]. To obtain this average value, different formulations can be applied and, depending on them, the result can have significant consequences on the final solution of the problem. In this section, these differences are analysed for the onset of localisation on a beam under pure bending.

On one hand, to compute the average strain at a certain Gauss point, the

contribution of each neighbour is weighted depending on its distance s to the Gauss point of interest. To obtain the weight α_0 for each contributing point, different weight functions can be used; in this study the following have been considered:

- Gaussian function

$$\alpha_0(s) = \exp\left(-\frac{s^2}{R^2}\right)$$

- Exponential function

$$\alpha_0(s) = \exp\left(-\frac{s}{R}\right)$$

- Bell-shaped function:

$$\alpha_0(s) = \left\langle 1 - \frac{s^2}{R^2} \right\rangle^2$$

where $\langle\cdot\rangle$ denotes the Macaulay brackets:

$$\langle x \rangle = \begin{cases} 0 & \text{if } x < 0 \\ x & \text{if } x \geq 0 \end{cases}$$

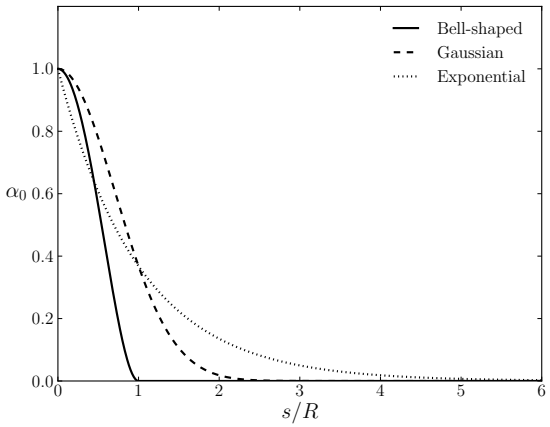

Figure 1: Weight functions considered in this study

The shape of these functions can be observed in Fig. 1. It is interesting to note that the bell-shaped function is equal to 0 for values of s greater than R,

while the other two, Gaussian and exponential functions, are extended beyond R, with the first of which being extended up to $\approx 2.5R$ and the second up to $\approx 6R$.

On the other hand, when close to a boundary, the area considered for averaging the strain value extends out of the body limits; to face this issue, the weight function can be scaled using different techniques. In this study, the following scaling techniques are considered:

- Standard scaling
- Local complement
- Distance-based scaling
- Stress-based scaling

2.1. Description of the nonlocal scaling options

The nonlocal strain is obtained using the following expression:

$$\bar{\varepsilon}(\boldsymbol{x}) = \int_V \alpha(\boldsymbol{x}, \boldsymbol{\xi}) \tilde{\varepsilon}(\boldsymbol{\xi}) \, \mathrm{d}\boldsymbol{\xi} \tag{1}$$

where $\boldsymbol{x}$ stands for the coordinates of the point where the nonlocal value is computed (it will be referred to as point of interest in the future), $\boldsymbol{\xi}$ for the coordinates of each of the points that contribute to the nonlocal value (which in the case of the bell-shaped function correspond to those at a distance $\leq R$; in the case of the Gauss function and the exponential function, these correspond to those at a distance $\leq 2.5R$ and $\leq 6R$, respectively) and $\tilde{\varepsilon}(\boldsymbol{\xi})$ for the equivalent strain at $\boldsymbol{\xi}$.

Therefore, this expression provides a weighted average of the local equivalent strain by integrating the value of the local equivalent strain $\tilde{\varepsilon}$ at each point $\boldsymbol{\xi}$ and applying a weight function α.

The weight values obtained with the expressions presented in section 2 are not normalised, so using them directly in (1) would result in an incorrect value,

since the following normalising condition must be imposed:

$$\int_{V_\infty} \alpha(\boldsymbol{x}, \boldsymbol{\xi}) \, \mathrm{d}\boldsymbol{\xi} = 1 \tag{2}$$

If this is imposed on an infinite body V_∞, it is sufficient to scale α_0 by a constant:

$$\alpha(\boldsymbol{x}, \boldsymbol{\xi}) = \frac{\alpha_0(\|\boldsymbol{x} - \boldsymbol{\xi}\|)}{V_{r\infty}} \tag{3}$$

where:

$$V_{r\infty} = \int_{V_\infty} \alpha_0(\|\boldsymbol{x} - \boldsymbol{\xi}\|) \, \mathrm{d}\boldsymbol{\xi} \tag{4}$$

This value can be analytically computed for each weight function, adopting the following values in each case:

- Bell-shaped function: $V_{r\infty} = \frac{\pi R^2}{3}$
- Gaussian function: $V_{r\infty} = \pi R^2$
- Exponential function: $V_{r\infty} = 2\pi R^2$

2.2. Boundary treatment

When the nonlocal value is computed near a boundary, the normalising condition (2) is not met using (3) and (4), since these are valid assuming that all the points in the volume surrounding the point of interest and delimited by R contribute to (1). Nevertheless, when the point of interest is close to a body boundary, the volume that contributes to (1) is reduced (see Fig. 2) and some considerations must be done in order to obtain the nonlocal strain at that point.

2.2.1. Standard scaling

Expression (3) uses (4) to normalise the value of α_0 provided by the corresponding weight function, assuming that all the points around the point of interest that are at a distance for which the weight is $\neq 0$ contribute in the

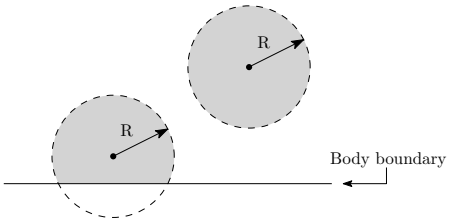

Figure 2: When the point of interest is near a boundary, the contributing volume (shaded in grey) is reduced.

nonlocal value obtained with (1). When the point of interest is near a boundary, some of these points do not contribute to (1) anymore and, to deal with this, the standard approach is to normalise the values of α by using only the values of α_0 that correspond to points that are inside the body. This leads to the following expression of the nonlocal strain:

$$\bar{\varepsilon}(\boldsymbol{x}) = \int_V \alpha(\boldsymbol{x}, \boldsymbol{\xi}) \tilde{\varepsilon}(\boldsymbol{\xi}) \, \mathrm{d}\boldsymbol{\xi} \tag{5}$$

where:

$$\alpha(\boldsymbol{x}, \boldsymbol{\xi}) = \frac{\alpha_0(\|\boldsymbol{x} - \boldsymbol{\xi}\|)}{V_r(\boldsymbol{x})} \tag{6}$$

and:

$$V_r(\boldsymbol{x}) = \int_V \alpha_0(\|\boldsymbol{x} - \boldsymbol{\xi}\|) \, \mathrm{d}\boldsymbol{\xi} \tag{7}$$

2.2.2. Local complement approach

Instead of normalising α by using V_r and not $V_{r\infty}$, the local complement approach consists of adding a term to the expression (3):

$$\alpha(\boldsymbol{x}, \boldsymbol{\xi}) = \frac{\alpha_0(\|\boldsymbol{x} - \boldsymbol{\xi}\|)}{V_{r\infty}} + \left(1 - \frac{V_r(\boldsymbol{x})}{V_{r\infty}}\right) \delta(\boldsymbol{x} - \boldsymbol{\xi})$$

where δ is the Dirac distribution. This leads to the following expression of the

nonlocal strain:

$$\bar{\varepsilon}(\boldsymbol{x}) = \frac{1}{V_{r\infty}} \int_V \alpha_0(\|\boldsymbol{x} - \boldsymbol{\xi}\|)\tilde{\varepsilon}(\boldsymbol{\xi})\ \mathrm{d}\boldsymbol{\xi} + \left(1 - \frac{V_r(\boldsymbol{x})}{V_{r\infty}}\right)\tilde{\varepsilon}(\boldsymbol{x}) \tag{8}$$

where $V_{r\infty}$ stands for the integral of α_0 extended to an infinite volume and can be obtained with (4).

2.2.3. Distance-based approach (linear expression of γ)

There exist different approaches to overcome the boundary problem based on the distance to the body limits [13, 14, 15]; here the distance-based nonlocal formulation described in [12] by Grassl et al. will be considered.

As well as in the standard scaling, the weight function is also scaled, but α_0 is made dependent on the minimum distance between the point where the nonlocal value is obtained and the nearer specimen boundary by including a function $\gamma(\boldsymbol{x})$. This formulation, as described in the referenced paper by Grassl et al., is implemented assuming an exponential weight function, therefore, the strategy consists of modifying the expression of the exponential function by multiplying R by the $\gamma(\boldsymbol{x})$ function:

$$\alpha_0(\boldsymbol{x}, \boldsymbol{\xi}) = \exp\left(-\frac{\|\boldsymbol{x} - \boldsymbol{\xi}\|}{\gamma(\boldsymbol{x})R}\right) \tag{9}$$

where:

$$\gamma(\boldsymbol{x}) = \begin{cases} 1 & \text{if} \quad d(\boldsymbol{x}) \geq tR \\ \dfrac{1-\beta}{tR} d(\boldsymbol{x}) + \beta & \text{if} \quad d(\boldsymbol{x}) < tR \end{cases} \tag{10}$$

In (10), t and β are internal parameters of this approach and $d(\boldsymbol{x})$ is the minimum distance of point $\boldsymbol{x}$ to the body boundary. For more details on this formulation, the reader is referred to [12].

If, instead of the exponential function, the bell-shaped weight function is used, the expression of α_0 turns to be as follows:

$$\alpha_0(\boldsymbol{x}, \boldsymbol{\xi}) = \left\langle 1 - \frac{\|\boldsymbol{x} - \boldsymbol{\xi}\|^2}{(\gamma(\boldsymbol{x}) \cdot R)^2} \right\rangle^2 \tag{11}$$

Finally, if a Gaussian weight function is used, the expression of α_0 reads:

$$\alpha_0(\boldsymbol{x}, \boldsymbol{\xi}) = \exp\left(-\frac{\|\boldsymbol{x} - \boldsymbol{\xi}\|^2}{(\gamma(\boldsymbol{x})R)^2}\right) \tag{12}$$

2.2.4. Distance-based approach (exponential expression of γ)

In [12], Grassl et al. found out that using an exponential expression for $\gamma(\boldsymbol{x})$, instead of the linear expression shown in (10), improves the results for the dissipated energy profile near the crack initiation region, eliminating the local peak near the boundary. The alternative exponential expression of $\gamma(\boldsymbol{x})$ proposed by Grassl et al. reads as follows:

$$\gamma(\boldsymbol{x}) = 1 - (1 - \beta)\exp\left(-\frac{d(\boldsymbol{x})}{tR}\right) \tag{13}$$

2.2.5. Stress-based approach

Here, again, different approaches based on the stress state of the material can be found [16, 17, 18] formulations can be found in the literature; in this study the one described in [12] will be considered.

This approach makes use of the following transformation matrix:

$$\mathbf{T} = \begin{pmatrix} 1 & 0 \\ 0 & \frac{1}{\gamma} \end{pmatrix} \begin{pmatrix} n_{1x} & n_{1y} \\ -n_{1y} & n_{1x} \end{pmatrix} = \begin{pmatrix} n_{1x} & n_{1y} \\ -\frac{n_{1y}}{\gamma} & \frac{n_{1x}}{\gamma} \end{pmatrix} \tag{14}$$

where n_{1x} and n_{1y} are the components of the unit eigenvector $\boldsymbol{n}_1$ associated to the maximum principal value of the effective stress $\tilde{\boldsymbol{\sigma}}$. This formulation, as described in [12], is implemented assuming an exponential weight function, therefore, the weight function reads:

$$\alpha_0(\boldsymbol{x}, \boldsymbol{\xi}) = \exp\left(-\frac{\|\mathbf{T}(\boldsymbol{x}) \cdot (\boldsymbol{\xi} - \boldsymbol{x})\|}{R}\right) \tag{15}$$

where:

$$\gamma = \begin{cases} \beta + (1 - \beta)\left(\dfrac{\langle\tilde{\sigma}_2\rangle}{\tilde{\sigma}_1}\right)^2 & \text{if} \quad \tilde{\sigma}_1 > 0 \\ 1 & \text{if} \quad \tilde{\sigma}_1 \leq 0 \end{cases} \tag{16}$$

In (16), β is an internal parameter of this formulation, $\tilde{\sigma}_1$ the first principal effective stress and $\tilde{\sigma}_2$ the second principal effective stress.

If a bell-shaped weight function is used, α_0 presents the following expression:

$$\alpha_0(\boldsymbol{x}, \boldsymbol{\xi}) = \left\langle 1 - \frac{\|\mathbf{T}(\boldsymbol{x}) \cdot (\boldsymbol{\xi} - \boldsymbol{x})\|^2}{R^2} \right\rangle^2 \tag{17}$$

And, finally, if a Gaussian weight function is used, α_0 reads as follows:

$$\alpha_0(\boldsymbol{x}, \boldsymbol{\xi}) = \exp\left(-\frac{\|\mathbf{T}(\boldsymbol{x}) \cdot (\boldsymbol{\xi} - \boldsymbol{x})\|^2}{R^2} \right) \tag{18}$$

3. Analytical study

To study how these formulations affect the onset of damage localisation in the pure bending problem, a simple analytical model has been developed. The description of this model as well as the assumptions made for it are described in the first subsection. In the second subsection, the implementation of each averaging procedure is defined and finally, in the third subsection, the results of this study are presented and commented.

3.1. Analytical model

Let us consider a rectangular section of height h subjected to pure bending using a nonlocal characteristic length equal to R. If we think of an infinitely long rectangular beam, we only need to consider a finite length of such beam in order to apply the nonlocal formulations described before. The geometry of the model is presented in Fig. 3.

The nonlocal strain is obtained for one section of the beam, called "section of interest" in the figure. In the longitudinal direction, the model is extended up to six times the nonlocal characteristic length ($6R$) so all the points that can contribute to the nonlocal averaged value are considered. Note that if the bell-shaped function is used, this distance can be reduced to R, but if the exponential or the Gaussian functions are used, this distance must be extended, since the points beyond a distance equal to R still contribute to the average value (see

Fig. 1). Although these functions never reach a value equal to 0, no matter how big s is, a value of $6R$ can be considered to be sufficient to cover all cases.

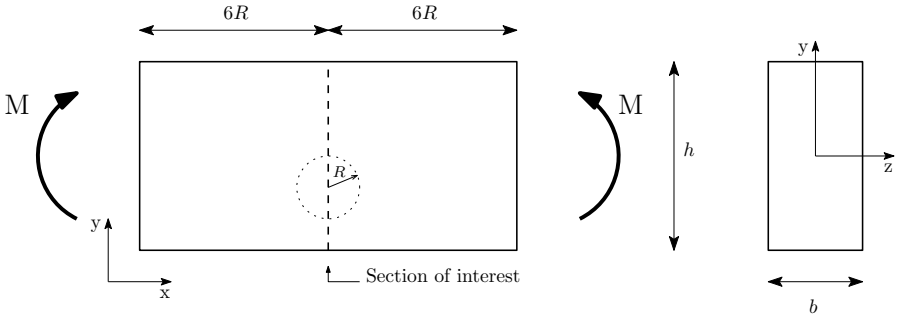

Figure 3: Geometry of the analytical model.

To compute the nonlocal average strain at a point in the socalled section of interest, the local values of the surrounding points must be considered. Under pure bending each point in the section of interest is esentially under tension, so the damage will be initiated when this longitudinal stress reaches a threshold value, which will first take place at the lower face of the section. In order to carry out this analytical study, the nonlocal longitudinal strain is computed using only the local longitudinal strains of the surrounding points, which, under pure bending and before damage localisation takes place, depend only on the y coordinate (see Fig. 3).

Under a certain bending moment M, the curvature is obtained assuming that under elastic conditions and before damage is initiated, Navier-Bernouilli hypothesis is valid, so a plane section before the moment is applied, remains plane after it:

$$\frac{1}{r} = \frac{M}{EI_z}$$

where E is the Young's modulus and I_z is the moment of inertia respect to the z axis.

This curvature leads to a linear distribution of the longitudinal strain along the cross section and the local equivalent strain $\tilde{\varepsilon}$ for each point in the grid can

be obtained.

3.2. Implementation of the averaging schemes

The averaging techniques described in section 2.2 have been implemented as follows:

3.2.1. Standard scaling

Equation (5) turns into the following expression:

$$\bar{\varepsilon}(\boldsymbol{x}) = \frac{\sum_V \alpha_0(\boldsymbol{\xi}) a(\boldsymbol{\xi}) \tilde{\varepsilon}(\boldsymbol{\xi})}{\sum_V \alpha_0(\boldsymbol{\xi}) a(\boldsymbol{\xi})} \tag{19}$$

where $a(\boldsymbol{\xi})$ represents the contributing area associated to each contributing point $\boldsymbol{\xi}$

3.2.2. Local complement approach

Equation (8) is numerically implemented as:

$$\bar{\varepsilon}(\boldsymbol{x}) = \frac{\sum_V \alpha_0(\boldsymbol{\xi}) a(\boldsymbol{\xi}) \tilde{\varepsilon}(\boldsymbol{\xi})}{V_{r\infty}} + \left(1 - \frac{\sum_V \alpha_0(\boldsymbol{\xi}) a(\boldsymbol{\xi})}{V_{r\infty}}\right) \tilde{\varepsilon}(\boldsymbol{x}) \tag{20}$$

where $V_{r\infty}$ is obtained as expressed in (4).

3.2.3. Distance-based approach

Nonlocal strain $\bar{\varepsilon}(\boldsymbol{x})$ is obtained with the following expression:

$$\bar{\varepsilon}(\boldsymbol{x}) = \frac{\sum_V \exp\left(-\dfrac{\|\boldsymbol{x} - \boldsymbol{\xi}\|}{\gamma(\boldsymbol{x}) R}\right) a(\boldsymbol{\xi}) \tilde{\varepsilon}(\boldsymbol{\xi})}{\sum_V \exp\left(-\dfrac{\|\boldsymbol{x} - \boldsymbol{\xi}\|}{\gamma(\boldsymbol{x}) R}\right) a(\boldsymbol{\xi})} \tag{21}$$

where γ is obtained with (10) if the linear formulation is chosen and with (13) if the exponential expression is preferred. To obtain γ, parameter t has been estimated to be equal to 1.00 and parameter β equal to 0.15, the same values used in [12].

3.2.4. Stress-based approach

Nonlocal strain $\bar{\varepsilon}(\boldsymbol{x})$ is obtained with:

$$\bar{\varepsilon}(\boldsymbol{x}) = \frac{\sum_V \exp\left(-\dfrac{\|\mathbf{T}(\boldsymbol{x})\cdot(\boldsymbol{\xi}-\boldsymbol{x})\|}{R}\right) a(\boldsymbol{\xi})\tilde{\varepsilon}(\boldsymbol{\xi})}{\sum_V \exp\left(-\dfrac{\|\mathbf{T}(\boldsymbol{x})\cdot(\boldsymbol{\xi}-\boldsymbol{x})\|}{R}\right) a(\boldsymbol{\xi})} \tag{22}$$

where the $\mathbf{T}$ tensor is computed by using the equation (14). As in [12], a value of $\beta = 0.15$ has been adopted to obtain γ.

It must be noted that in the specific case of pure bending, the unit eigenvector $\boldsymbol{n}_1$ is always coincident with the unit vector in the x axis direction, therefore: $\boldsymbol{n}_1 = (1\ 0)$ in the cartesian coordinate system in 2d. This means that matrix $\mathbf{T}$ always reads:

$$\mathbf{T} = \begin{pmatrix} 1 & 0 \\ 0 & \frac{1}{\gamma} \end{pmatrix}$$

Regarding the expression of γ, under pure bending, $\tilde{\sigma}_2$ is always ≤ 0, therefore, expression (16), in our case always reads:

$$\gamma = \begin{cases} \beta & \text{if} \quad \tilde{\sigma}_1 > 0 \\ 1 & \text{if} \quad \tilde{\sigma}_1 \leq 0 \end{cases}$$

3.3. Results

The grid used in this numerical study counts with 121 horizontal points by 201 vertical points. The cross section is considered to have a height of $h = 0.080$m and a width of $b = 0.001$m. The section is under a bending moment equal to 1 N·m and the material is defined as elastic, with a Young modulus of $20000 MPa$.

As Fig. 1 shows, the specific meaning of R clearly depends on the weight function used, since the same value of R will result in very different contributing areas to the computation of the nonlocal value, with the one corresponding to the bell-shaped function being the smaller of them and the exponential function being the largest. Therefore, to allow for comparison of the results obtained

with different weight functions, equivalent values of R must be identified, which can be done by using the concept of radius of inertia around the y axis:

$$r_y = \int_0^\infty r^2 \alpha(r) dr \tag{23}$$

To ensure an equivalent contributing area for obtaining the nonlocal value at each point, a value of R equal to 0.004 has been set for the bell-shaped function and the corresponding values for the Gaussian and the exponential functions have been obtained so that the radii of inertia around the y axis, defined as in (23), are equal in all three cases. As a result, values of R equal to 0.004 mm, 0.00166 mm and 0.000782 mm have been used for the bell-shaped function, the Gaussian function and the exponential function, respectively.

Figs. 4, 5 and 6 show the elastic strain profile in red and the nonlocal strain profiles in various colours for the following cases:

- Influence of different scaling formulations near the boundaries using the exponential weight function (Fig.4).
- Influence of different scaling formulations near the boundaries using the Gaussian weight function (Fig.5).
- Influence of different scaling formulations near the boundaries using the bell-shaped weight function (Fig. 6).

In all three cases, the nonlocal strain profiles obtained using the standard scaling, the local complement technique, the distance-based approach with linear γ, the distance-based approach with exponential γ and the stress-based approach are compared.

Fig. 4 presents the results for different scaling formulations using the exponential weight function and clearly shows how the standard scaling provides a strain profile that deviates from the elastic strain profile near the boundary. The local complement formulation, however, provides a profile that differs less from the elastic one, whereas the distance-based and the stress-based formulations give a much closer value next to the boundary. Regarding the distance-based

a)

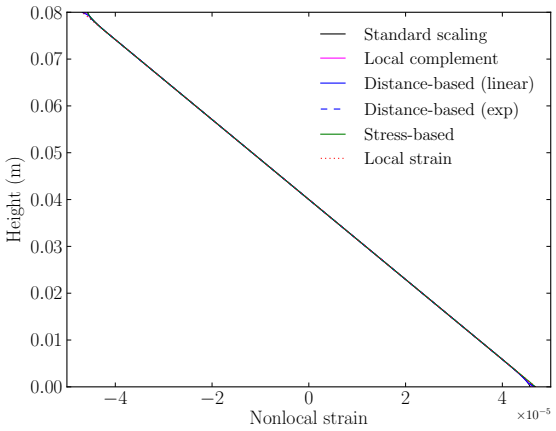

b)

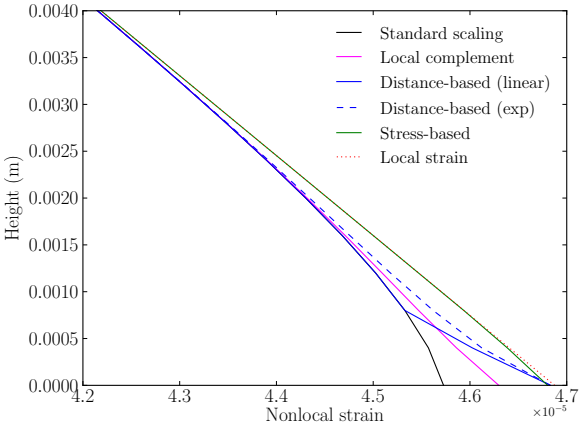

Figure 4: Profiles of nonlocal strains using different averaging techniques and the exponential weight function: a) Complete profile, b) Detail near the lower boundary (under tension).

a)

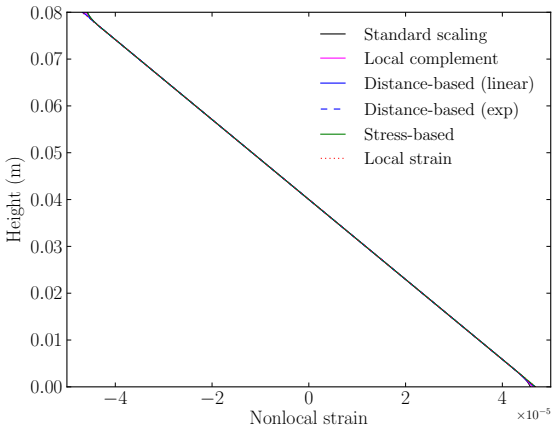

b)

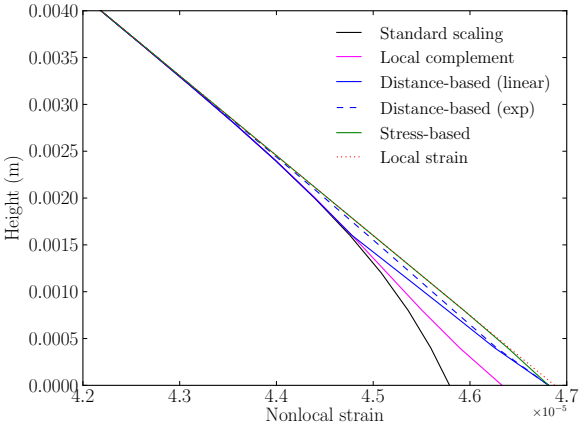

Figure 5: Profiles of nonlocal strains using different averaging techniques and the Gaussian weight function: a) Complete profile, b) Detail near the lower boundary (under tension).

a)

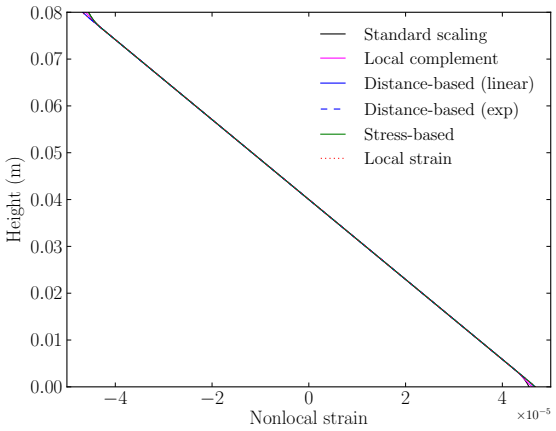

b)

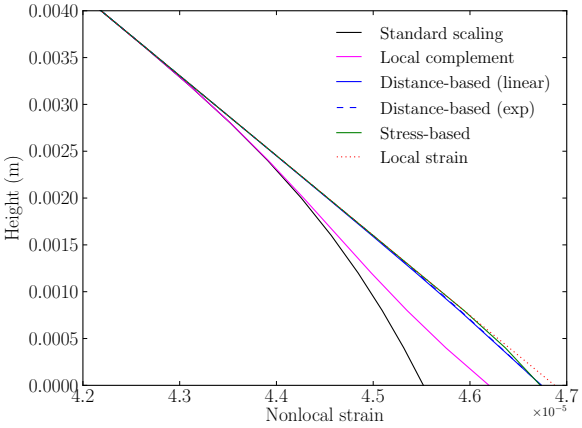

Figure 6: Profiles of nonlocal strains using different averaging techniques and the bell-shaped weight function: a) Complete profile, b) Detail near the lower boundary (under tension).

approach, when the linear expression of γ is used, its behaviour is coincident with the standard scaling procedure up to a distance equal to R ($= 0.000782$m in this case, since these results make use of the exponential weight function), then the prediction gets closer to the elastic profile in the last region, close to the boundary. This is due to the fact that the formulation of the distance-based approach coincides with the standard scaling formulation up to that point and is modified by γ only for points that are at a distance to the boundary $\leq R$, therefore providing closer results to the elastic predition. Nevertheless, when the exponential expression (13) is used for γ, its behaviour is smoother since the same formula is used along the whole section of interest. In summary, although both, the distance-based and the stress-based approaches, clearly provide profiles that are more similar to the elastic prediction at the boundary, the latter provides a closer profile all along the cross section, only being slightly different when the point is very close to the boundary.

Fig. 5 shows the results for different scaling approaches using the Gaussian weight function. Results of the standard and local complement techniques are very similar to those in Fig. 4, again clearly differing from the elastic profile. As in Fig. 4, both distance-based approaches and especially the stress-based approach provide profiles that are very similar to the elastic prediction, with the latter only differing in the very last part of the curve, near the boundary.

Fig. 6 presents the results for different scaling approaches using the bell-shaped function. Results of the standard and local complement techniques do not differ much from those in Figs. 4 and 5, although in general it can be noted that the profiles are a bit more different to the elastic prediction than in the previous Figures. Regarding the distance-based approaches and the stress-based approach, they again provide profiles that are closer to the elastic prediction but now even closer in the case of both distance-based techniques.

4. Numerical simulations

This section describes the numerical work carried out to analyse the behaviour of the nonlocal formulations presented before in this paper. All the finite element models have been developed using OOFEM [21, 22, 23] and, since the effect of the weight function has already been observed in the analytical study, here the focus will be on the scaling techniques, assuming always a bell-shaped weight function.

In the first subsection the geometry of the model and the boundary and loading conditions are described, the second subsection describes the material formulation, the third subsection presents the results obtained for each nonlocal formulation and several values of the characteristic length and finally, the fourth subsection studies the localisation problem for longer beams, were damage localises in more than one area.

4.1. Geometry and boundary conditions

The aim of this model is to assess the localisation properties of nonlocal damage models under pure bending. To do this, a constant cross section beam subjected to a uniformly distributed bending moment and zero normal force is considered. The beam is assumed to be very long and boundary effects that might be introduced by the supports at the end sections are eliminated by imposing periodic boundary conditions.

Fig. 7 shows the main features of this model. If a local formulation were used, only defining master and slave planes at both, right and left boundaries, would be sufficient, but since nonlocal formulations are used, integration points very close to these planes would lack of data because they would try to collect values from neighbours that do not exist in the model. To solve this issue, nonlocal interaction is considered not only for the real neighbours but also for their periodic images. Therefore, if we look at Fig. 7, to compute the nonlocal value at point B, not only those integration points placed at a distance $\leq R$ from B are considered, but also those at a distance $\leq R$ from B', which is the periodic image of B at the left of the model.

The only boundary condition to be imposed is a fixed support at one node and, as already mentioned, the load is introduced by defining an imposed rotation angle ϕ (see Fig. 8).

A regular mesh is used, with 20 vertical elements and a variable number of horizontal elements in each model; all the elements are always 1.0 mm wide and 4.0 mm high.

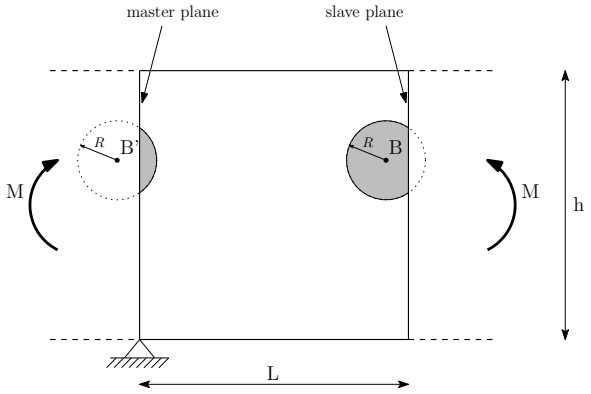

Figure 7: Scheme of the numerical model.

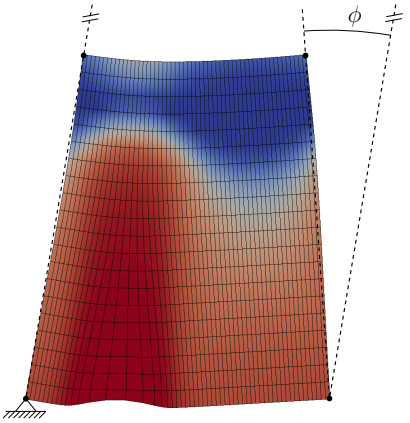

Figure 8: Imposed rotation angle ϕ. Note that the displacements have been magnified by a factor of 100 to make the angle noticeable.

4.2. Material

The material is defined as elastic and an isotropic damage model is used. In this model, the stiffness degradation is isotropic and the stiffness damaged tensor is expressed as $\boldsymbol{D} = (1 - \omega)\boldsymbol{D}_e$ where ω represents a scalar damage variable and $\boldsymbol{D}_e$ the elastic stiffness tensor.

The damage evolution is defined by the following exponential softening law:

$$\omega = 1 - \frac{\varepsilon_0}{\varepsilon} \exp\left(-\frac{\varepsilon - \varepsilon_0}{\varepsilon_f - \varepsilon_0}\right)$$

where ε_0 is the strain at peak stress, which defines the beginning of the softening process and ε_f is a value of strain that controls the ductility of the softening branch (see Fig. 9).

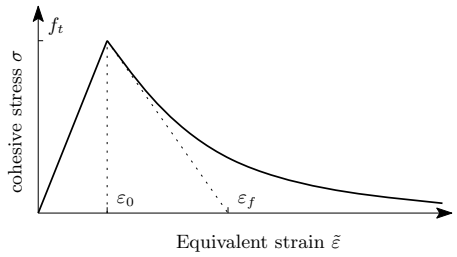

Figure 9: Scheme of the stress-strain diagram used in the damage model.

All these values of strain correspond to scalar measures obtained from the strain tensor and using Mazar's definition of equivalent strain [24]:

$$\tilde{\varepsilon} = \sqrt{\sum_{I=1}^{3} \langle \varepsilon_I \rangle^2}$$

where $\langle \varepsilon_I \rangle$ stands for the positive parts of the principal values of the strain tensor.

The material is defined with an elastic modulus of $E = 20000$ MPa, a Poisson's coefficient of $\nu = 0.20$ and the following damage parameters: $\varepsilon_0 = 1.2{\cdot}10^{-4}$ and $\varepsilon_f = 7.0 \cdot 10^{-3}$.

Since the material is completely uniform in the whole model, to trigger localisation, a random very small perturbation in the displacements field (of

the order of 10^{-8} mm) is imposed in two nodes of the lower boundary of the beam. This techniques proves to be sufficient to induce damage localisation in the model.

4.3. Results

Under pure bending, the solution initially remains uniform in each fibre parallel to the beam axis and, when damage begins to develop, it starts to concentrate in bands equally spaced each from another. Fig. 10 show these bands at the onset of localisation for a model that represents a long periodic cell where eight localisation bands are formed; parameter s identifies the bands spacing.

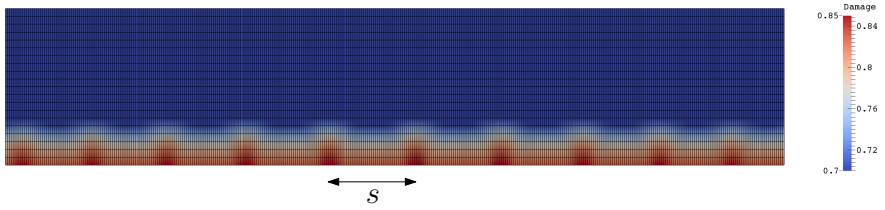

Figure 10: Localisation bands spaced at a distance s.

The localisation pattern, i.e. bands spacing distance s, is affected by the specific boundary treatment used as well as the value of the characteristic length R. To study this, the five averaging schemes presented previously are considered: standard scaling, local complement, distance-based approach with a linear expression of γ, distance-based approach with an exponential expression of γ and stress-based approach. To observe how the characteristic length affects the localisation pattern, six values of R are considered for each of these schemes: 3 mm, 4 mm, 5 mm, 6 mm, 7 mm and 8 mm.

In order to define the value of s that corresponds to a specific combination of characteristic length R and averaging scheme, the following strategy is followed: different lengths of the periodic cell are considered (parameter L in Fig. 7), always using the same element dimensions 1 mm $\times$ 4 mm and modifying the number of horizontal elements in the grid. The value of s corresponds to the

model for which the localisation develops at a lower value of the applied bending moment. Table 1 summarises the results obtained following this procedure and Fig. 11 shows them plotted.

R	**3 mm**	**4 mm**	**5 mm**	**6 mm**	**7 mm**	**8 mm**
Standard scaling	42	47	51	55	60	67
Distance-based (linear γ)	40	43	47	51	54	57
Distance-based (exponential γ)	35	38	41	43	46	47
Stress-based	43	48	53	57	64	74
Local complement	40	45	49	53	58	64

Table 1: Localisation spacing s for different values of R and each averaging scheme. Units in mm.

According to Fig. 11, increasing the characteristic length increases the band spacing, but not all the averaging schemes are equally sensitive to the value of R. Standard scaling, local complement approach and stress-based approach are highly sensitive to this while band spacing using distance-based approaches shows a much smaller dependence on the characteristic length.

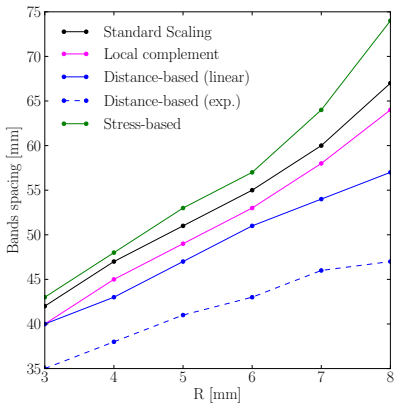

Figure 11: Localisation bands spacing s dependence on the characteristic length R.

Fig. 12 shows the Moment-$\frac{\phi}{L}$ diagrams for several values of the characteristic

length, with $\frac{\phi}{L}$ being the parameter that represents the imposed rotation angle at the master plane (see Fig. 8) normalised by the length L of the periodic cell. Each diagram presents the corresponding curves for a specific value of R and all the averaging schemes considered in this study.

These results suggest that an increasing value of R slightly increase the ductile response of the model, which is reasonable since increasing the value of R leads to an average value of the nonlocal strain $\bar{\varepsilon}$ that is computed using strain values at points that are further from the damage developing area. Note that $\bar{\varepsilon}$ is the value that drives the damage in the material model, so including lower values of equivalent strain to compute it, like those of points further from the damaged zone, will result in a delay of the damage development.

In all cases, no matter the value of R, distance-based approaches provide an earlier softening process than in the rest of the averaging schemes, with the exponential γ distance-based approach being the earliest of them and, interestingly, leading to a more progressive decrease of the bending moment.

Fig. 13 presents the dissipated energy profiles along the cross section of the beam where the fracture is developed comparing different averaging schemes for different values of R. On one hand, since some models lead to computational instabilities for very high damage states, not all of them can reach the final state where the whole cross section is fully damaged; to allow for comparison, the dissipated energy is obtained for the instant corresponding to a bending moment of 450 N·mm. These results show that the distance-based approaches, especially the one using an exponential expression for γ, dissipate smaller amounts of energy during the fracture process. Surprisingly, unlike Grassl et al. observed in [12], the stress-based scheme dissipates more energy than the other approaches, even compared with the standard approach. In the paper by Grassl et al. three-point bending tests on notched specimens were studied and, unlike pure bending on constant cross section beam, stress concentration is very high near the notch, which could be the reason for the differences observed here.

Diagrams in Figures 12 and 13 must be carefully compared, because one can be tempted to compare the areas under the graphs in Figure 12 with the

dissipated energy profiles in Figure 13 and expect good agreement between them. They are not directly comparable, since the latter presents the dissipated energy per localised zone, that is to say, per beam length where localisation is encapsulated (equal to the localisation bands spacing), which is different for each averaging scheme and for each value of R. That is why, for instance, in the case of the exponential γ distance-based models, the areas under the graphs in Figure 12 are larger than for the rest of the averaging schemes and in Figure 13 it is smaller, since the localisation zone is significantly narrower in this case.

4.4. Localisation on longer beams

So far, the smallest beam length for which damage localisation takes place for the minimum value of the bending moment has been studied, therefore, in all the previous models, damage localises only in one place. If the beam is longer, then damage tends to localise in more than one region, although usually only one of them fully develops until failure.

To study this, three beam models are compared: a model for which damage localises in one single area for the minimum value of the bending moment ($L =$ 38 mm), a model of a beam twice longer ($L = 76$ mm) and a model of a beam four times longer ($L = 152$ mm); in all of them, the distance-based averaging scheme with an exponential expression of γ has been used and a value of R equal to 4 mm has been set. Figure 14 shows how damage localises in each of these models. In all three cases, the pictures show the damaged beam at a bending moment equal to 2500 N·mm after peak; damage evolves in all these models up to a very low value of the bending moment, close to 0, but it has been considered more convenient to show the evolution damage at an intermediate state, so that the localisation areas can be easily identified.

Looking at the first two models, damage localisation can be easily identified in one area when $L = 38$ mm and in two equally spaced areas when $L = 76$ mm. In the case of the 76 mm long beam, localisation takes place at two areas at the same time and develop at the same rate up to a curvature value for which only one of them develops until failure.

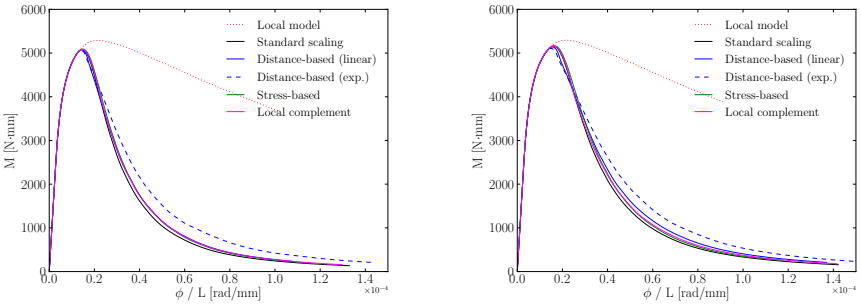

a)

b)

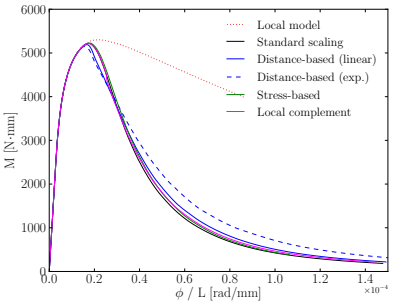

c)

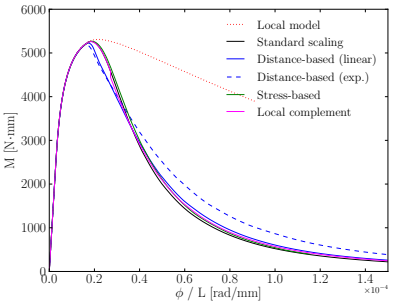

d)

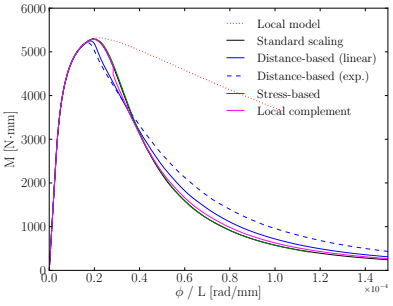

e)

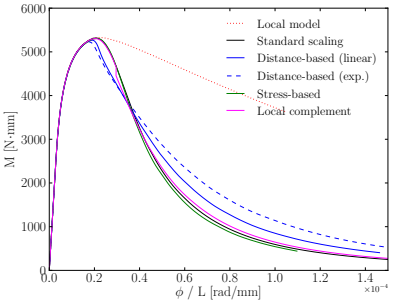

f)

Figure 12: M-$\frac{\phi}{L}$ diagrams for different values of R: a) R = 3mm b) R = 4mm c) R = 5mm d) R = 6mm e) R = 7mm f) R = 8mm.

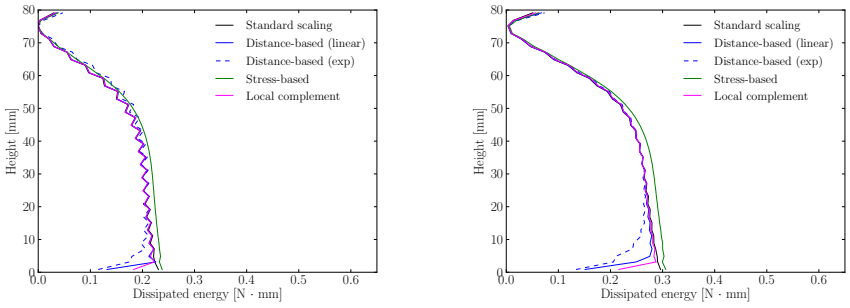

a)

b)

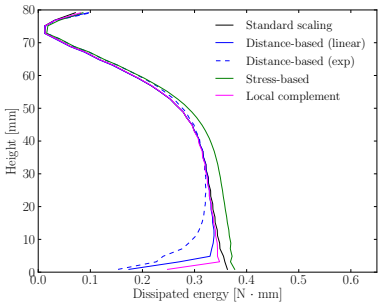

c)

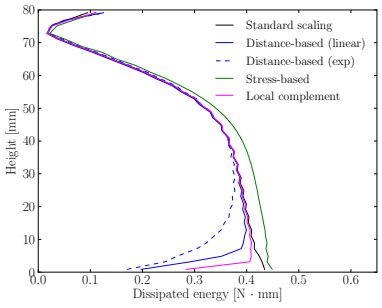

d)

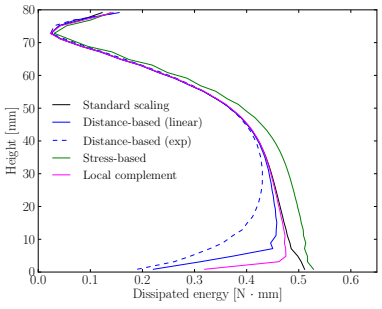

e)

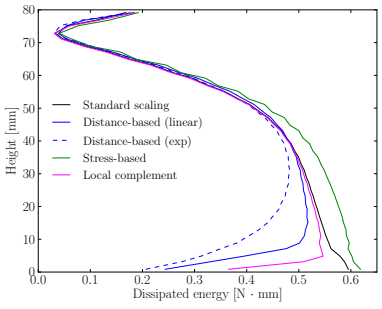

f)

Figure 13: Dissipated energy diagrams per localisation zone for different values of R: a) R = 3mm b) R = 4mm c) R = 5mm d) R = 6mm e) R = 7mm f) R = 8mm. The energy value corresponds to a zone width equal to the band spacing for each case.

a)

b)

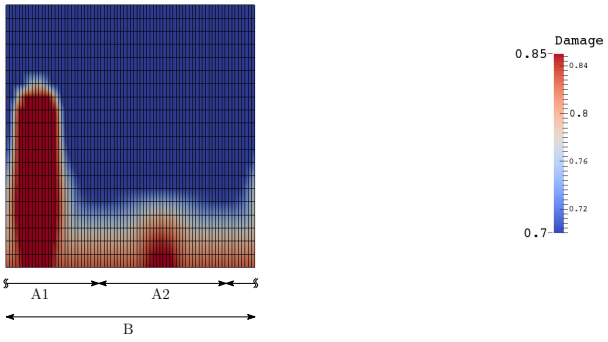

c)

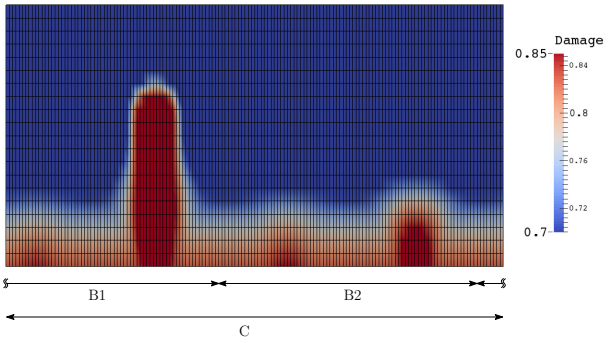

Figure 14: Damage localisation in beams with different lengths: a) $L = 38mm$, b) $L = 76mm$, c) $L = 152mm$.

In the case of the longer beam, with $L = 152$ mm, damage localises in four equally spaced areas at the same time in an early stage and develop at the same rate up to a curvature value for which damage only grows in two of them. Finally, when a certain curvature is reached, damage keeps on growing in only one of the two, eventually leading to failure. It is interesting to note that the second localisation process takes place in alternate areas (positions two and four in the Figure).

The moment-curvature diagrams of these models, with the curvature expressed by $\frac{\phi}{L}$, are compared in Figure 15 where a detail of the diagram around the zone of maximum bending moment is also provided. It can be observed how the second localisation process deviates curves blue and red, which correspond to $L = 76$ mm and $L = 152$ mm, from the black line, which corresponds to the base model, $L = 38$ mm. Also, it can be identified the point where the red line deviates from the blue one due to the third localisation process.

Now, looking again at Figure 14, if A identifies the base periodic cell for which localisation first takes place and B identifies the periodic cell that is twice as long as A, in Figure 14b, A2 perturbs the total value of $\frac{\phi}{L}$ compared to that in Figure 14a, since once the second localisation process starts it experiences a smaller relative rotation of its left and right limits than that of A1. For the same reason, if C identifies the periodic cell that is twice as long as B (and thus four times longer than A), in Figure 14c, the portion B2 perturbs the total value of $\frac{\phi}{L}$ from the instant when the third localisation process develops, experiencing a smaller relative rotation than B1, where the localisation process continues until failure. All this explains why for consecutive localisation processes in longer beams, the M-$\frac{\phi}{L}$ diagram tends to present a snapback behaviour after peak.

Finally, Figure 16 presents the dissipated energy for each of the three models, which proves that, although damage is quite generalised at the lower part of the beam, the energy dissipation is very localised in the crack that eventually develops.

a)

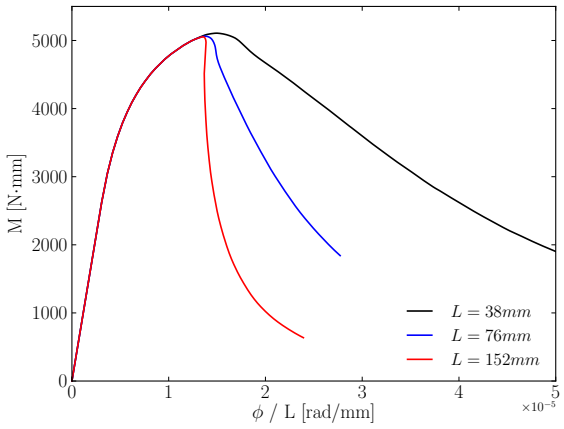

b)

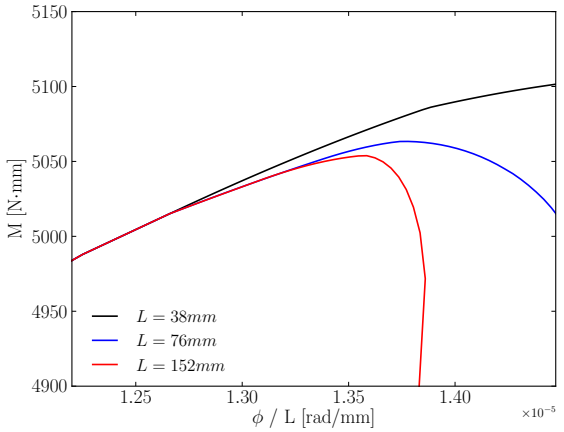

Figure 15: M-$\frac{\phi}{L}$ diagrams for beams with different lengths: a) complete graph, b) detail of the maximum bending moment zone.

a)

b)

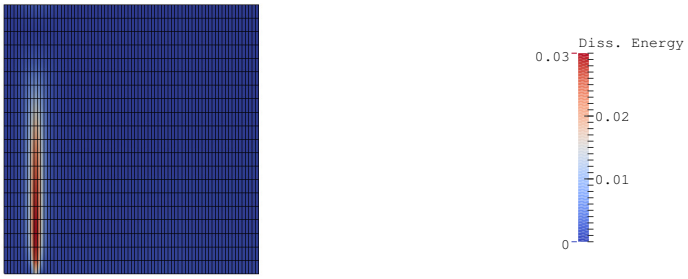

c)

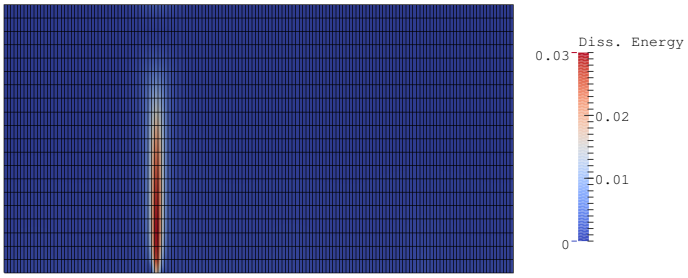

Figure 16: Dissipated energy density in beams with different lengths: a) $L = 38$ mm, b) $L = 76$ mm, c) $L = 152$ mm.

4.5. Example: damage due to shrinkage

So far, a beam under pure bending has been analysed, which can be seen as an unrealistic problem, since bending forces usually go together with tension and compression forces. Nevertheless, pure bending can be understood as a load case where the strain field evolves in parallel planes accross the beam, which is a not an unusual loading case in structural elements; temperature gradients and shrinkage are examples of such cases.

In this section, a concrete beam under shrinkage is studied. Figure 17 shows a sketch of the 2D model, where the effect of shrinkage is analysed on a 10 mm-thick rectangular beam with the longitudinal displacement and rotation blocked at both ends. Humidity is equal to 100% inside the beam and at the upper boundary, while it is equal to 20% at the lower boundary; any other boundary, left, right and in-plane boundaries, are impermeable environments. Therefore, as time goes by, beam humidity will gradually reduce at the lower boundary, giving rise to shrinkage effects that will induce strain increments in concrete, thus inferring tensile forces and, eventually, leading to structural damage and fracture.

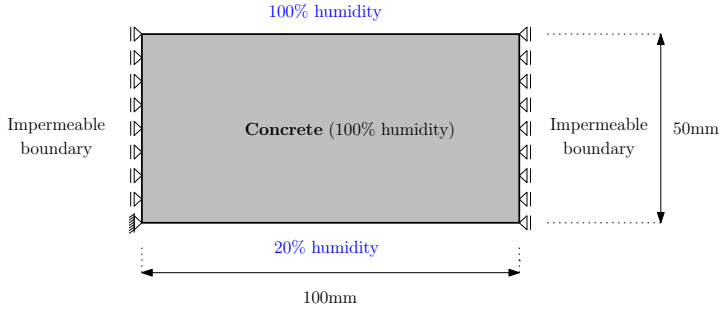

Figure 17: Model to study the effect of shrinkage on a concrete beam.

This problem is analysed by means of a staggered scheme. Therefore, as Figure 18 shows, two models are run in parallel, one to study the moisture transport problem and another one to study the evolution of damage in concrete. At each time step, first the transport problem is solved and the information about the moisture content inside the beam (w_i) is transferred to the structural

model which, using the moisture variation to compute the corresponding strain increment, solves the structural problem, where one of the nonlocal formulations addressed in this paper is used.

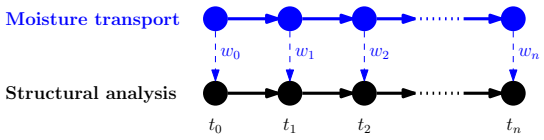

Figure 18: Scheme of the staggered problem.

The moisture transport problem is based on a nonlinear sorption isotherm, which relates the pore relative humidity h and the water content w, and on a humidity-dependent moisture permeability. All is governed by the following differential equation:

$$k(h)\frac{\partial h}{\partial t} = \nabla \cdot [c(h)\nabla h]$$

where k(h) is the humidity dependent moisture capacity [kg/m^3] and $c(h)$ is the moisture permeability [kg/m·s].

Here, a linear isotherm has been used, with a slope equal to 10^{-7} and the Bazant-Najjar permeability function [25] has been chosen to define the moisture permeability. Thus, the permeability function is described by equation (24).

$$C(h) = C_1 \left(\alpha_0 + \frac{1-\alpha_0}{1+\left(\frac{1-h}{1-h_c}\right)^n} \right) \tag{24}$$

where C_1 is the moisture diffusivity at full saturation, α_0 a dimensionless ratio of diffusivity at low humidity to diffusivity at full saturation, h_c the relative humidity at which the diffusivity is exactly between its minimum and maximum value and n a dimensionless exponent. Here the following values of these parameters have been adopted: $C_1 = 15 \cdot 10^{-7}$ kg/m·s, $\alpha_0 = 0.1$, $h_c = 0.75$ and $n = 10$.

To reproduce the structural behaviour, the elastic behaviour of the material has been defined by a Young's modulus $E = 20000$ MPa and a Poisson's ratio $\nu = 0.20$, whereas the damage evolution is defined by the following parameters:

$\varepsilon_0 = 1.2 \cdot 10^{-4}$ and $\varepsilon_f = 7.0 \cdot 10^{-3}$. The exponential γ distance-based averaging scheme has been used, with a bell-shaped weight function and the following internal parameters: $t = 1.00$, $\beta = 0.15$.

Finally, the strain variation due to shrinkage is computed using the relative humidity variation obtained in the transport model, which are related by a constant factor k_{sh}:

$$\dot{\varepsilon}_{sh} = k_{sh}\dot{h} \tag{25}$$

In this process, the relative humidity is obtained by means of the sorption isotherm defined by Pedersen [26], which requires three parameters that are calibrated experimentally: w_h, n and a. Here, the following values are adopted: $k_{sh} = 0.0025$, $w_h = 0.0476$, $n = 0.182$ and $a = 4.867$. Note that these values have not been obtained for a specific case, but are reasonable values to illustrate the effect of shrinkage on the evolution of damage in concrete, which is the purpose of this section.

Figure 19 shows the evolution of damage at different times, expressed in days. At $t = 0.634$, damage is concentrated in a number of zones equally spaced from each other, at $t = 2.266$ damage keeps on evolving in four of them, while it stops in the others, at $t = 4.526$, damage only grows in two cracks and, finally, at $t = 31.857$, damage develops only in one crack that crosses the beam from side to side, leading to the eventual structural failure of the beam. It is interesting to note how, as observed in the study on beams under pure bending, damage evolves gradually on a smaller number of cracks, always evenly distributed, leaving frozen cracks in between that do not evolve anymore. It must also be noted that at $t = 31.857$, damage can also be observed in the upper boundary, but the origin of such damage is completely different to that observed in the lower boundary, since it is not due to shrinkage, but to the crack opening that induces a certain displacement and infers tensile forces at the upper sides of the right and left boundaries.

a) $t = 0.634$

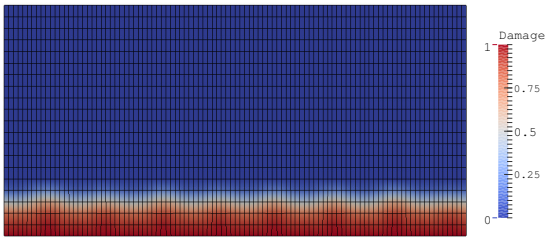

b) $t = 2.266$

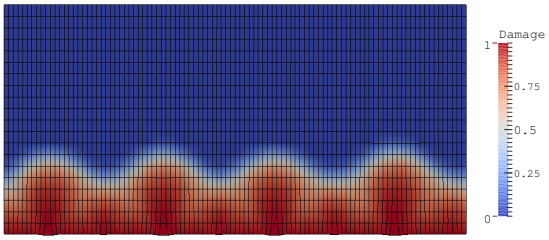

c) $t = 4.526$

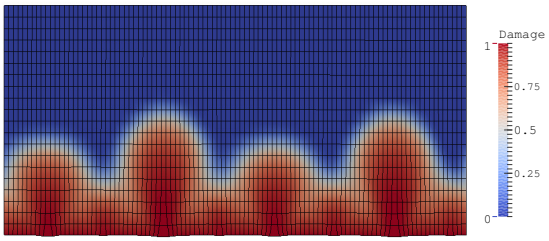

d) $t = 31.85$

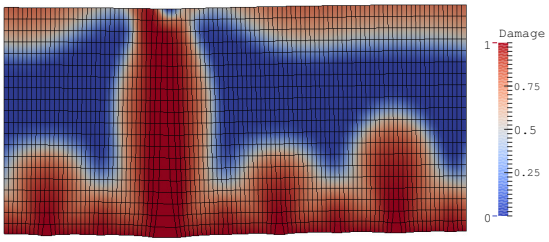

Figure 19: Damage evolution in the beam due to the effect of shrinkage at different times (time in days).

5. Conclusions

This paper has analysed the localisation of damage in quasibrittle materials when a nonlocal approach is used for the specific case of a beam under pure bending. The influence of three main aspects have been addressed in this study: the weight function, the averaging scheme applied near the boundaries and the value of the characteristic length.

An analytical approach has served to understand how the nonlocal strain is computed in each of them, which determines when the damage starts to develop, since damage is triggered for an initial value of the equivalent strain ε_0. This study has shown that for all weight functions considered here, the stress-based and both distance-based approaches provide a nonlocal strain profile closer to the elastic response, while the standard approach provides significantly lower values near the boundary with respect to the elastic profile, and the local complement an intermediate profile between that provided by the standard scheme and the elastic one.

Finite element simulations have served to model a periodic cell representing a beam under pure bending. This approach has been used to understand how each averaging scheme and the value of the characteristic length affect the localisation bands spacing that can be observed when running a model for a long beam (see Figure 10). Each averaging scheme has proved to be sensitive to the value of the characteristic length, with the stress-based approach being the most sensitive and the exponential γ distance-based approach the least sensitive of them; as expected, an increasing value of the characteristic length results in a higher ductility of the model which can be observed in the load-curvature diagrams shown in Figure 12 and, hence, in a higher dissipated energy value, which can be observed in Figure 13.

Finally, in order to study a more realistic case of damage localisation under

a uniformly distributed increase of strain, damage localisation due to shrinkage on a concrete beam has been analysed. Shrinkage induces a strain variation in a structure which also develops in parallel planes, like a pure bending case but, of course, with a different strain gradient. This study has been addressed by using a staggered approach, thus, modelling the transport problem and the damage problem independently and running them in parallel; then after each time step, the transport problem provides the moisture content inside the beam, which is used by the structural problem to compute the evolution of damage.

Ackowledgements

This work has been supported by the European Union under the project on Support of Inter-Sectoral Mobility and Quality Enhancement of Research Teams at the Czech Technical University in Prague (CZ.1.07/2.3.00/30.0034).

The author wishes to express his gratitude to Prof. Milan Jirásek, without whose supervision and wise advice this work would have never been done.

References

[1] Z. P. Bazant, S. Baweja, Creep and shrinkage prediction model for analysis and design of concrete structures: Model b3, ACI Special Publications 194 (2000) 1–84.

[2] N. Gardner, Comparison of prediction provisions for drying shrinkage and creep of normal-strength concretes, Canadian Journal of Civil Engineering 31 (5) (2004) 767–775.

[3] K. Sakata, T. Shimomura, Recent progress in research on and code evaluation of concrete creep and shrinkage in japan, Journal of Advanced Concrete Technology 2 (2) (2004) 133–140.

[4] P. Havlásek, M. Jirásek, Modeling of concrete creep based on microprestress-solidification theory, Acta Polytechnica 52 (2) (2012)

34–42, cited By 7.
URL https://www.scopus.com/inward/record.uri?eid=2-s2.0-84860682263&partnerID=40&md5=41c442b3af0e823d8f620bebc013408b

[5] P. Havlásek, Creep and shrinkage of concrete subjected to variable environmental conditions, Ph.D. thesis (2014).

[6] Z. P. Bazant, M. Jirásek, M. Hubler, I. Carol, Rilem draft recommendation: Tc-242-mdc multi-decade creep and shrinkage of concrete: material model and structural analysis. model b4 for creep, drying shrinkage and autogenous shrinkage of normal and high-strength concretes with multi-decade applicability, Materials and structures 48 (4) (2015) 753–770.

[7] P. Havlásek, M. Jirásek, Multiscale modeling of drying shrinkage and creep of concrete, Cement and Concrete Research 85 (2016) 55–74.

[8] Z. P. Bažant, M. Jirásek, Nonlocal integral formulations of plasticity and damage: survey of progress, Journal of Engineering Mechanics 128 (11) (2002) 1119–1149.

[9] J. Planas, M. Elices, G. Guinea, Cohesive cracks versus nonlocal models: Closing the gap, International Journal of Fracture 63 (2) (1993) 173–187.

[10] P. Havlásek, P. Grassl, M. Jirásek, Analysis of size effect on strength of quasi-brittle materials using integral-type nonlocal models, Engineering Fracture Mechanics 157 (2016) 72 – 85. doi:http://dx.doi.org/10.1016/j.engfracmech.2016.02.029.
URL http://www.sciencedirect.com/science/article/pii/S0013794416300455

[11] M. Jirásek, S. Rolshoven, P. Grassl, Size effect on fracture energy induced by non-locality, International journal for numerical and analytical methods in geomechanics 28 (7-8) (2004) 653–670.

[12] P. Grassl, D. Xenos, M. Jirásek, M. Horák, Evaluation of nonlocal approaches for modelling fracture near nonconvex boundaries, International Journal of Solids and Structures 51 (18) (2014) 3239–3251.

[13] J. Bolander Jr, H. Hikosaka, Simulation of fracture in cement-based composites, Cement and Concrete Composites 17 (2) (1995) 135–145.

[14] A. Krayani, G. Pijaudier-Cabot, F. Dufour, Boundary effect on weight function in nonlocal damage model, Engineering Fracture Mechanics 76 (14) (2009) 2217–2231.

[15] Z. Bažant, J.-L. Le, C. G. Hoover, Nonlocal boundary layer (nbl) model: overcoming boundary condition problems in strength statistics and fracture analysis of quasibrittle materials, Fracture Mechanics of Concrete and Concrete Structures—Recent Advances in Fracture Mechanics of Concrete, B.-H. Oh, Ed., Korea Concrete Institute, Seoul (2010) 135–143.

[16] Z. P. Bažant, Nonlocal damage theory based on micromechanics of crack interactions, Journal of engineering mechanics 120 (3) (1994) 593–617.

[17] M. Jirásek, Z. P. Bažant, Localization analysis of nonlocal model based on crack interactions, Journal of engineering mechanics 120 (7) (1994) 1521–1542.

[18] C. Giry, F. Dufour, J. Mazars, Stress-based nonlocal damage model, International Journal of Solids and Structures 48 (25) (2011) 3431–3443.

[19] C. Polizzotto, Remarks on some aspects of nonlocal theories in solid mechanics, in: Proceedings of the 6th National Congr. SIMAI, 2002.

[20] G. Borino, B. Failla, F. Parrinello, A symmetric nonlocal damage theory, International Journal of Solids and Structures 40 (13) (2003) 3621–3645.

[21] B. Patzák, Oofem project home page, URL http://www. oofem. org.

[22] B. Patzák, Z. Bittnar, Design of object oriented finite element code, Advances in Engineering Software 32 (10) (2001) 759–767.

[23] B. Patzák, Oofem—an object-oriented simulation tool for advanced modeling of materials and structures, Acta Polytechnica 52 (6).

[24] J. Mazars, Application de la mécanique de l'endommagement au comportement non linéaire et à la rupture du béton de structure, Ph.D. thesis (1984).

[25] Z. Bažant, L. Najjar, Nonlinear water diffusion in nonsaturated concrete, Materiaux et Construction 5 (1) (1972) 3–20.

[26] C. Rode, Combined heat and moisture transfer in building constructions, Ph.D. thesis, Technical University of Denmark (DTU) (1990).